Gold Nanoparticles with Tipped Surface Structures as Substrates for Single-Particle Surface-Enhanced Raman Spectroscopy: Concave Nanocubes, Nanotrisoctahedra, and Nanostars

Qingfeng Zhang,[†] Nicolas Large,[‡,§] and Hui Wang*,[†]

[†]Department of Chemistry and Biochemistry, University of South Carolina, 631 Sumter Street, Columbia, South Carolina 29208, United States

[‡]Department of Electrical and Computer Engineering, Laboratory for Nanophotonics, Rice University, Houston, Texas 77005, United States

S *Supporting Information*

ABSTRACT: We demonstrate that Au nanoparticles with tipped surface structures, such as concave nanocubes, nanotrisoctahedra, and nanostars, possess size-dependent tunable plasmon resonances and intense near-field enhancements exploitable for single-particle surface-enhanced Raman spectroscopy (spSERS) under near-infrared excitation. We report a robust seed-mediated growth method for the selective fabrication of Au concave nanocubes, nanotrisoctahedra, and nanostars with fine-controlled particle sizes and narrow size distributions. Through tight control over particle sizes, the plasmon resonances of the nanoparticles can be fine-tuned over a broad spectral range with respect to the excitation laser, allowing us to systematically quantify the SERS enhancements on individual nanoparticles as a function of particle size for each particle geometry. Understanding of the geometry-dependent plasmonic characteristics and SERS activities of the nanoparticles is further enhanced by finite-difference time-domain (FDTD) calculations. Our results clearly show that strong SERS enhancements can be obtained and further optimized on individual Au nanoparticles with nanoengineered "hot spots" on their tipped surfaces when the plasmon resonances of the nanoparticles are tuned to the optimal spectral regions with respect to the excitation laser wavelength. Using tunable plasmonic nanoparticles with tipped surface structures as substrates for spSERS represents a highly promising and feasible approach to the optimization of SERS-based sensing and imaging applications.

KEYWORDS: *surface-enhanced Raman spectroscopy, plasmon resonances, noble metal nanoparticles, concave nanocubes, nanotrisoctahedra, nanostars, finite-difference time-domain*
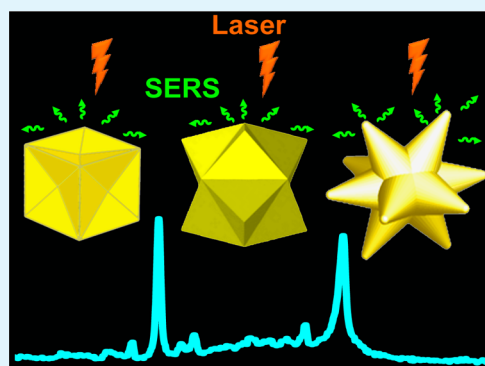
1. INTRODUCTION

Surface-enhanced Raman scattering (SERS) is an ultrasensitive vibrational spectroscopic technique capable of providing detailed structural information on the molecules on or in the vicinity of nanostructured metallic surfaces.[1,2] As a powerful, noninvasive spectroscopic tool for the detection of low-abundance analytes, SERS plays pivotal roles in food safety inspection,[3,4] environmental monitoring,[5] and biomolecular sensing.[6–8] By combining metallic nanoparticles with molecular Raman reporters, multifunctional SERS nanoprobes or SERS tags have been developed to target specific biomolecules both in vitro and in vivo, enabling Raman-based optical bioimaging with high spatial resolution and excellent photostability.[9–12] SERS is essentially a nanoscale effect directly related to the intense electromagnetic field enhancements generated at nanostructured metallic surfaces upon the excitation of localized surface plasmon resonances (LSPRs).[1,13] Due to strong plasmonic coupling effects,[14] aggregated or self-assembled metallic nanoparticles possess "hot spots" for SERS inside the sub-10 nm interparticle gaps with gigantic local-field enhancements, several orders of magnitude higher than those commonly achievable on individual nanoparticles.[14–17] Although it is possible to detect the Raman signals of just a few or even single molecules inside the tiny interparticle junctions,[18–20] these hot spots account for only a small portion of the total surface areas accessible by the analyte molecules, resulting in huge heterogeneity and poor reproducibility of Raman signals across the entire substrates.[21] The challenges associated with precise control over the spatial distribution, enhancement magnitude, and structural robustness of interstitial hot spots limit the utilization of nanoparticle aggregates as reliable and reproducible SERS substrates for sensing and imaging applications. For in vivo bioimaging, it is also highly desirable to use individual plasmonic nanoparticles uniformly appended with Raman reporters as the SERS tags rather than using the nanoparticle aggregates.[22–24] Therefore,

single-particle (sp) SERS represents a more promising approach to SERS-based sensing and imaging with optimizable signal amplification and reproducibility in comparison to those strategies relying on nanoscale interparticle junctions.

The plasmonic field enhancements of individual nanoparticles can be optimized through deliberate control over particle geometries.[13,25,26] While individual Au or Ag solid nanospheres exhibit modest field enhancements upon plasmonic excitation, multilayered metallic nanoparticles, also known as nanomatryoshkas, possess intraparticle SERS hot spots confined inside the narrow interior gaps.[22,27,28] Although individual multilayered nanoparticles may serve as excellent SERS probes for bioimaging, the interior intraparticle gaps are not readily accessible by the analyte molecules when used for SERS sensing. Individual nanoparticles with hot spots exposed on their outer surfaces are thus more appealing for molecular sensing applications. A widely used strategy of achieving intense field enhancements on the outer surfaces of individual nanoparticles is to controllably introduce nanoscale tipped or spiky features to the particle surfaces.[29−40] Upon plasmonic excitation, the electromagnetic fields are enormously enhanced at the surface vertices and edges, providing SERS hot spots on open surfaces that are easily accessible by molecules. A variety of Au or Ag nanoparticles with tipped surface features, such as surface-textured nanospheres,[29−33] etched nanopolyhedra,[34] multibranched nanostars,[35−38] and spiky nanoshells,[39,40] have all been shown to exhibit intense SERS enhancements on individual particles, convincingly demonstrating that the interparticle or intraparticle gap geometries are not always essential for strong SERS enhancements.

Another key design objective in spSERS optimization is to tailor the LSPRs of individual nanoparticles relative to the excitation laser wavelength,[41,42] because the on-resonance excitations typically generate much higher Raman enhancements than the off-resonance excitations. However, the far-field extinction maximum does not overlap exactly with the wavelength at which the largest near-field enhancements are achieved. Van Duyne and co-workers[42] observed that, on Ag nanoparticle arrays, maximum SERS enhancement was achieved when the far-field plasmon band position was red-shifted compared to the excitation laser wavelength. In contrast to this result, more recent experimental observations and electrodynamic calculations on various metallic nanostructures showed that maximum near-field enhancements occurred at lower energies than the corresponding far-field LSPRs.[43−48] Such a red shift of the near-field peak energies with respect to the far-field resonance energies has been predicted to be a universal phenomenon for metallic nanostructures and can be theoretically interpreted by a driven and damped harmonic oscillator model.[44] The relative spectral shift between near- and far-field resonances of plasmonic nanoantennas, however, depends strongly upon the size and shape of the nanoparticles[43−48] and thus needs to be further investigated more systematically and quantitatively on a wider variety of metallic nanostructures.

Here we study the far-field and near-field plasmonic properties of individual Au nanoparticles of three geometries—concave nanocubes, nanotrisoctahedra, and nanostars—with a particular focus on their performance as substrates for spSERS under near-infrared excitation. These three Au nanostructures all possess tipped surface features and size-dependent LSPRs, allowing us to fine-tune their LSPRs with respect to the excitation laser wavelength and to

quantitatively evaluate the size-dependent SERS enhancements on individual nanoparticles. The experimentally observed geometry dependence of far- and near-field plasmonic properties is further corroborated by finite-difference time-domain (FDTD) calculations. These Au nanoparticles with tunable LSPRs in the near-infrared "water window" and nano-engineered hot spots on their tipped surfaces hold great promise as single-particle nanosensors and nanoprobes for SERS-based biosensing and bioimaging applications.

2. RESULTS AND DISCUSSION

2.1. Shape-Controlled Synthesis of Au Concave Nanocubes, Nanotrisoctahedra, and Nanostars. Control over particle geometries allows one to fine-tune the LSPRs and surface properties of Au nanoparticles to match specific applications. For face-centered cubic (fcc) Au nanoparticles, the low-index {111} and {100} facets have lower surface energies and are thus, thermodynamically much more stable than {110} and other high-index facets.[49] As a consequence, Au nanoparticles enclosed by low-energy facets, such as nanocubes enclosed by six {100} facets, nanooctahedra enclosed by eight {111} facets, and multitwinned quasi-spherical nanoparticles with multifaceted surfaces enclosed by {111} and {100} facets, represent the most common nanoparticle geometries that are experimentally realizable. It has been recently demonstrated that Au nanoparticles of more complex geometries enclosed by various high-index facets can be fabricated through deliberate control over the nanoparticle growth kinetics and/or selective surface passivation.[50−57] Here we focus on three nanoparticle geometries with tipped surface structures: concave nanocubes, nanotrisoctahedra, and nanostars. As illustrated in Scheme 1,

Scheme 1. Geometries of Au Concave Nanocube, Nanotrisoctahedron, Nanostar, Nanocube, Nanooctahedron, and Multitwinned Quasi-Spherical Nanoparticle
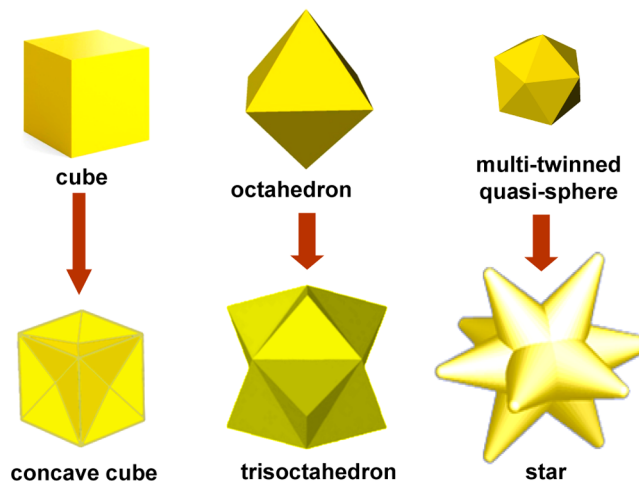

the concave nanocube is considered to be derived from a nanocube upon introduction of tetragonal indentation to each {100} facet. A nanotrisoctahedron can be obtained by adding convex trigonal pyramids to each {111} facet of a nano-octahedron. By growing nanoscale tips perpendicular to each exposed facet of a multitwinned quasi-spherical core, a multibranched star-shaped nanoparticle can be obtained. As demonstrated in greater detail later in this paper, Au concave nanocubes, nanotrisoctahedra, and nanostars exhibit significantly enhanced plasmonic tunability and improved perform-

ances as substrates for spSERS in comparison to the geometrically simpler nanocubes, nanooctahedra, and quasi-spherical nanoparticles.

As illustrated in Scheme 2, we adopted a seed-mediated growth method for the shape-selective fabrication of mono-

Scheme 2. Shape-Controlled Synthesis of Au Nanotrisoctahedra, Concave Nanocubes, and Nanostars through Seed-Mediated Nanoparticle Growth
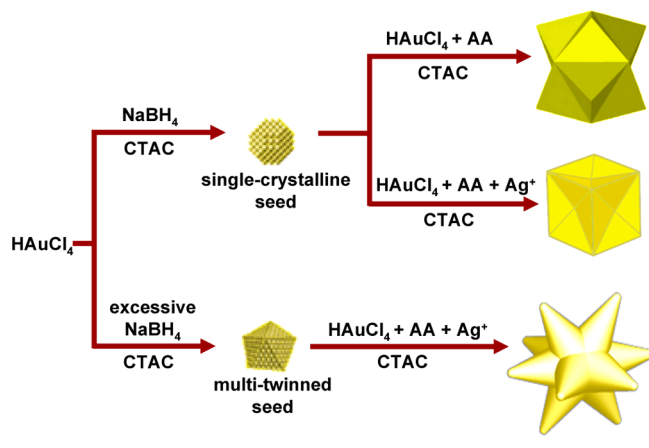
disperse Au concave nanocubes, nanotrisoctahedra, and nanostars. From single-crystalline quasi-spherical Au seeds, Au nanotrisoctahedra were obtained through kinetically controlled seed-mediated nanocrystal growth. As demonstrated in previous publications,[51,52,55,58] the Au nanotrisoctahedron is a kinetically favored geometry resulting from fast nanoparticle growth processes, while slower growth kinetics favors the formation of thermodynamically more stable geometries such as nanocubes, nanooctahedra, and quasi-spherical nanoparticles. Interestingly, by introduction of an appropriate amount of Ag^+ into the reaction mixtures, Au concave nanocubes were obtained as a result of the selective passivation of Au surfaces by Ag^+.[56] Changing the single-crystalline seeds to multitwinned seeds allowed for the fabrication of multibranched Au nanostars. As a consequence, the Au nanostars had multi-twinned crystalline structures while the nanotrisoctahedra and concave nanocubes were both single-crystalline in nature. The capability to fine-control the particle size for each geometry allowed us to gain detailed, quantitative insights into the size-dependent plasmonic properties and spSERS performances of the nanoparticles.

2.2. Au Concave Nanocubes. The concave nanocube is an interesting geometry with 24 equivalent indented facets whose Miller indices are determined by the degree of indentation. Figure 1A shows a transmission electron microscopy (TEM) image of Au concave nanocubes with average edge length of ∼130 nm. Each concave nanocube appeared to exhibit darker contrast in the interior regions compared to the edge regions. Concave nanocubes with different orientations with respect to the TEM grid exhibited different overall projection profiles and contrast evolution across the particle cross sections in the TEM images. The morphology of concave nanocubes was also characterized by scanning electron microscopy (SEM). The tetragonal indentation and the boundaries between adjacent indented facets both can be clearly visualized in the SEM image taken on one individual concave nanocube (inset, Figure 1A). Low-magnification SEM image (Figure S1A in Supporting
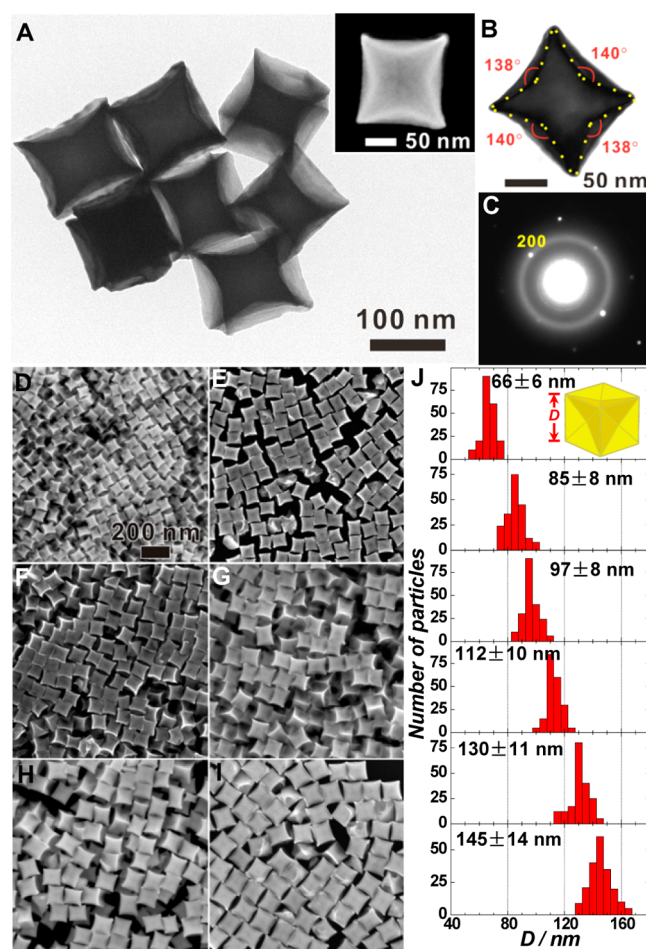
Figure 1. (A) TEM image of Au concave nanocubes with average edge length, *D*, of 130 nm. (Inset) SEM image of one individual concave nanocube. (B) TEM image of one individual concave nanocube with electron beam projected along the [001] direction. Measured dihedral angles between the concave facets are marked. (C) SAED pattern obtained from the particle in panel B. (D−I) SEM images of Au concave nanocubes with different average edge lengths obtained by adding (D) 0.5, (E) 0.1, (F) 0.05, (G) 0.025, (H) 0.015, and (I) 0.01 mL of Au seed solution. (J) Histograms showing the size distributions of Au concave nanocubes shown in panels D−I.

Information) further reveals that the as-fabricated Au concave nanocubes were highly monodisperse in terms of both particle size and morphology. Figure 1B shows the TEM image of one concave nanocube imaged with the electron beam projected along the [001] zone axis. The particle orientation and single-crystalline fcc structures of the concave nanocube were further verified by selected area electron diffraction (SAED) (Figure 1C). While the Au concave nanocube appeared to have a cubic morphological outline, the degree of indentation could be characterized by measuring the indentation angle (dihedral angle between indented facets) on the basis of different contrast in the TEM image. As marked in Figure 1B, the average indentation angle was measured to be ∼139°, indicating that each Au concave nanocube was enclosed by 24 high-index {830} facets. The as-fabricated particles exhibited a higher degree of indentation in comparison to the Au concave nanocubes enclosed by {720} facets (indentation angle of 148°) fabricated by Mirkin and co-workers.[56] As shown in Figure 1D−J, we were able to fine-control the edge lengths of the concave nanocubes in the range from ∼50 nm to over 150

nm by simply adjusting the amount of Au seeds added into the growth solutions. Unlike some other seeded growth methods through which the nanoparticles evolve into different morphologies as the particle size increases,[59,60] the concave cubic morphology of the particles fabricated by this protocol was well preserved throughout the entire particle size tuning range.

Au concave nanocubes displayed size-dependent tunable LSPRs. Figure 2A shows extinction spectra of colloidal Au
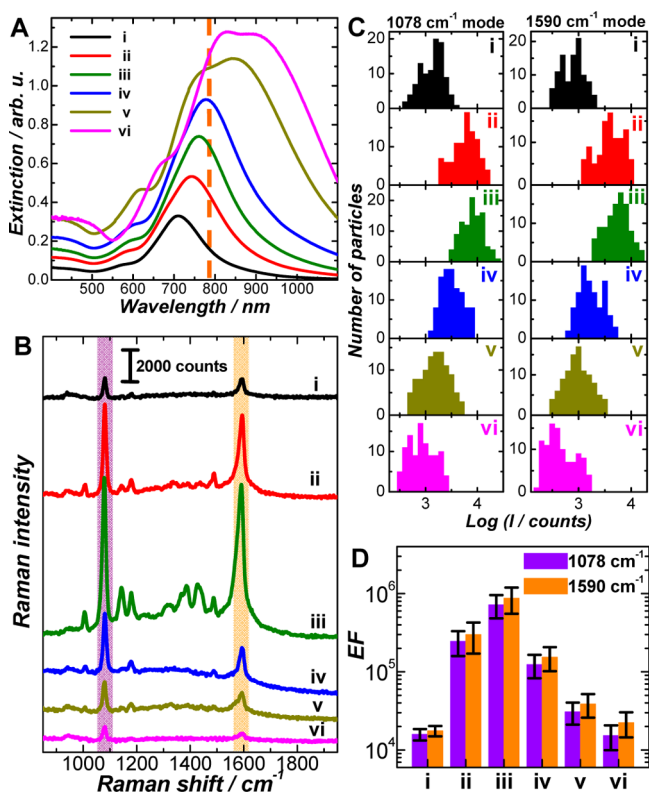

Figure 2. (A) Experimental extinction spectra of colloidal Au concave nanocubes of various sizes at a particle concentration of ~1.0 × 10⁹ particles·mL⁻¹. Vertical dashed line shows the excitation laser wavelength (785 nm) for Raman measurements. (B) Representative SERS spectra of 4-ATP adsorbed on individual concave nanocubes of various sizes. (C) Histograms of Raman intensities of 1078 and 1590 cm⁻¹ modes obtained from individual concave nanocubes. (D) SERS enhancement factors (EF) on individual concave nanocubes at 785 nm excitation. Labels i−vi in all panels correspond to concave nanocube samples shown in Figure 1D−I, respectively.

concave nanocubes of various average edge lengths at a particle concentration of ~1.0 × 10⁹ particles·mL⁻¹. As the particle size increased, the LSPRs progressively red-shifted and the extinction intensities at the resonance wavelengths increased. For Au concave nanocubes in the sub-100 nm size regime, the extinction spectra were dominated by a single-peaked dipolar plasmon band, while multiple peaks were observed when the edge lengths were beyond 100 nm. In comparison to Au nanocubes of the same edge lengths, Au concave nanocubes displayed significantly red-shifted LSPRs and more complex spectral line shapes in the optical extinction spectra. It has been reported that Au concave nanocubes exhibit greatly improved SERS performance in comparison to Au nanocubes and nanospheres of same size due to the intense local-field enhancements at sharp tips.[61] In addition to the particle

geometries, the coupling between LSPRs and the excitation laser is also a key factor that determines SERS enhancements. The size-dependent LSPRs of concave nanocubes allowed us to fine-tune their LSPRs with respect to the excitation laser wavelength and quantify the spSERS enhancements as a function of particle size.

To measure spSERS, a submonolayer of isolated Au concave nanocubes was immobilized on a poly(4-vinylpyridine)-functionalized glass substrate[40,62] and was used as substrate for spSERS measurements (see Figure S1B,C in Supporting Information). Because of the tipped surface features, only a small portion of the concave nanocube surface was in contact with the substrates. We also sandwiched a thin layer of water between two glass coverslips during SERS measurements to ensure that the dielectric medium surrounding the surface-immobilized Au nanoparticles was water. Therefore, the presence of the glass substrates had minimal effects on the plasmon resonance frequencies of the surface-immobilized concave nanocubes, as shown in Figure S2 in Supporting Information. The individual nanoparticles were well separated from each other, with interparticle distances much larger than the size of each particle. Therefore, interparticle plasmonic coupling was negligible and should have no contribution to the Raman enhancement. The large interparticle distances allowed us to focus the laser beam on one particle each time, using a confocal Raman microscope to collect spSERS signals. The synthesized ensembles showed relatively narrow size distributions (see Figure 1J), which led to standard inhomogeneous broadening of the LSPRs. Therefore, the size distribution of colloidal particles should not introduce significant modifications to the SERS resonant conditions.

4-Aminothiophenol (4-ATP) was chosen as a Raman reporter for the quantification of SERS enhancements because it is a nonresonant molecule with minimal chemical enhancements under near-infrared excitation and forms uniform self-assembled monolayers (SAMs) on Au surfaces with known packing density.[63] 4-ATP molecules were immobilized onto Au nanoparticle surfaces through evaporation of 20 µL of 1.0 mM ethanolic solution of 4-ATP over the substrate surface at room temperature. The evaporation of 1 mM 4-ATP ethanolic solution (20 µL) took about 20 min, which was found to be sufficient for the 4-ATP molecules to form nicely packed SAMs on the Au nanoparticle surfaces. Incubation of surface-immobilized nanoparticles with 1 mM 4-ATP for 24 h resulted in essentially the same spectral features and peak intensities in the SERS spectra, as shown in Figure S3 in Supporting Information. Here we fine-tuned the plasmon resonance wavelengths with respect to a fixed laser excitation wavelength at 785 nm. Excitations at shorter wavelengths in the visible region may activate charge-transfer processes that contribute to the chemical enhancements. In addition, excitation at shorter wavelengths may also facilitate plasmon-mediated photo-reactions of 4-ATP as reported previously.[64] Therefore, we decided to use this near-infrared excitation to minimize the resonance enhancements, chemical enhancements, and photo-reactions, allowing us to particularly focus on only the electromagnetic contribution to the Raman enhancements.

Figure 2B shows the representative SERS spectra of 4-ATP adsorbed on individual Au concave nanocubes of various sizes. Two intense Raman bands at 1078 and 1590 cm⁻¹ were observed in the SERS spectra, corresponding to the C−S stretching mode and phenol ring C−C stretching mode, respectively.[15] We collected SERS spectra of 4-ATP SAMs on

Au concave nanocubes from more than 100 individual particles for each sample one particle at a time. The intensity histograms of the 1078 and 1590 cm^{-1} bands are shown in Figure 2C. Maximum SERS signals were obtained on the sample whose far-field plasmon band position was blue-shifted by ∼30 nm in wavelength with respect to the excitation laser. Murphy and co-workers[48] have recently observed a similar trend on colloidal suspensions of plasmonically tunable Au nanorods, and they interpreted their results as a consequence of competition between plasmon-enhanced Raman scattering and light reabsorption along the propagation pathway through the colloidal samples. Interestingly, we observed the same trend on surface-immobilized submonolayers of concave nanocubes where reabsorption effects were negligible, strongly indicating that the blue shift of LSPRs relative to the optimal excitation wavelengths should be a universal feature for metallic nanoparticles regardless of whether they are immobilized on a surface or suspended as colloids. The largest SERS enhancements were observed on nanoparticles of around 100 nm in size whose extinction was dominated by scattering rather than absorption. We further estimated the enhancement factors (EFs) by comparing SERS signals to normal Raman intensities obtained from neat 4-ATP films (Figure S4 in Supporting Information). As shown in Figure 2D, the phenol ring C−C stretching mode showed larger enhancements than the C−S stretching mode, most likely due to the stronger coupling between the transition dipole moment and local electric field. The EFs were estimated to be on the order of 10^4–10^5, approaching 10^6 when the LSPR was tuned to the optimal spectral region with respect to the excitation laser. Similar EFs have also been achieved on individual Au porous nanoparticles as reported in a recently published paper.[58] These estimated EFs were averaged over the entire particle surfaces. The local enhancements in the hot spots at the tips, however, are anticipated to be at least 1 or 2 orders of magnitude higher.

To more quantitatively understand how the variation in edge length and side-facet indentation affect the plasmonic properties of Au concave nanocubes, we used the finite-difference time-domain (FDTD) method to calculate the far-field extinction and near-field enhancements of individual concave nanocubes. To more precisely match the experimental particle geometry, corner curvatures of 5 nm in radius were introduced to the nanocubes and concave nanocubes. Each face of the concave nanocubes exhibited a sharp tetragonal indentation of angle θ. Figure 3A shows the calculated extinction spectral evolution of a Au concave nanocube (edge length of 112 nm) as the indentation angle changes from 180° for a nanocube gradually to 125° for a highly indented concave nanocube. The far-field extinction spectra were calculated with the incident plane-wave polarized along the edge, the face diagonal, and the body diagonal of the nanocube, respectively. For all three polarizations, the LSPRs progressively red-shifted and the spectral line shapes became increasingly more complex, with multipeaked features gradually developed as the degree of indentation increased. This is in line with previous observations that Au concave nanocubes display significantly red-shifted LSPRs in comparison to Au nanocubes of the same sizes.[61] As shown in Figure 3B, the concave nanocubes exhibited highest field enhancements in the vicinities of the tips, and electric fields were significantly enhanced at the particle edges as well. Larger field enhancements were achieved on the surfaces of concave nanocubes with higher degrees of indentation. SERS enhancement factors are proportional to $|E/E_0|^4$ under certain
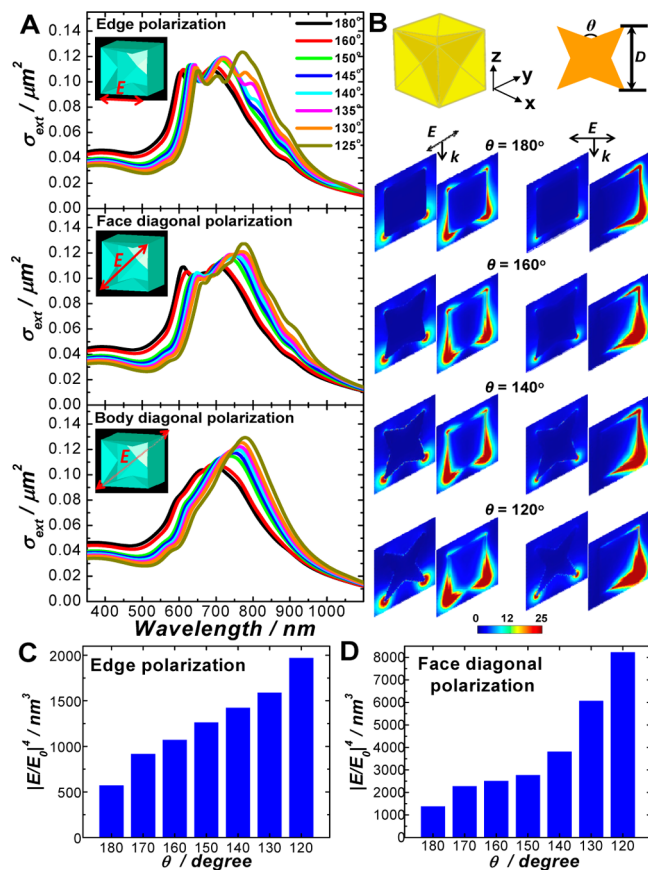

Figure 3. (A) Calculated extinction spectra of Au concave nanocube (D = 112 nm) with varying indentation angles (θ) for three polarizations (edge, face-diagonal, and body-diagonal polarizations). (B) Cross-sectional views of calculated near-field enhancements ($|E/E_0|^2$) of Au concave nanocubes with edge length 112 nm and various indentation angles of 180°, 160°, 140°, and 120° at 785 nm excitation. The geometry of a concave nanocube in three-dimensional Cartesian coordinates and the cross-section of the concave nanocube in the yz plane are illustrated. The left column is edge polarization, and the right column is face-diagonal polarization. The incident plane wave propagates along the z-axis, and the body center of the concave nanocube is at $x = y = z = 0$. Two planes parallel to the yz plane at $x = 0$ and 56 nm are shown for each polarization and indentation angle. (C, D) Fourth power of the field enhancements integrated over volume ($|E/E_0|^4$) of concave nanocube (D = 112 nm) with various indentation angles for (C) edge and (D) face-diagonal polarizations.

approximations. To assess the SERS enhancements from individual concave nanocubes based on the FDTD results, we calculated the integrated fourth power of the field enhancements, $|E/E_0|^4$, over the entire volume up to 1.5 nm above the cube faces. While the electric field enhancement $|E/E_0|$ is unitless, the integrated $|E/E_0|^4$ over volume has a unit of cubic nanometers. The integrated $|E/E_0|^4$ values were dependent on both local field enhancements and total size of the nanoparticles. The relative values of integrated $|E/E_0|^4$ provide useful information for us to compare the SERS performances of different nanoparticles. As shown in Figure 3C,D, the integrated field enhancements increased with increasing degree of indentation for both the edge and face-diagonal polarizations.

In Figure 4A, we compare the calculated extinction spectra of Au concave nanocubes with fixed indentation angle of 140° and various edge lengths. To take into account the ensemble effects
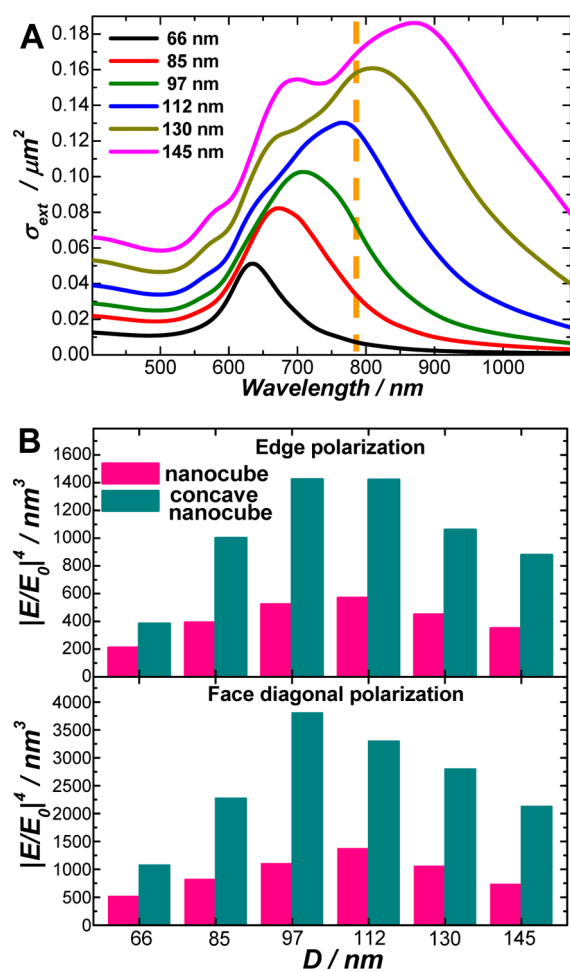
Figure 4. (A) Calculated extinction spectra of concave nanocube with indentation angles of 140° and varying edge lengths as labeled in the figure. Vertical dashed line shows the excitation laser wavelength (785 nm) for Raman measurements. (B) Fourth power of the field enhancements integrated over volume ($|E/E_0|^4$) of concave nanocubes with $\theta = 140°$ and $D = 66$, 85, 97, 112, 130, and 145 nm and of a nonindented nanocube of the same sizes. (Upper panel) Edge polarization; (lower panel) face-diagonal polarization.

of randomly oriented nanoparticles in colloidal suspensions, FDTD-calculated extinction spectra were averaged over three polarizations, that is, edge, face-diagonal, and body-diagonal polarizations. The calculated extinction spectra were also averaged for three different indentations, $\theta = 140° \pm 5°$, to account for the inhomogeneous indentations of the experimentally fabricated samples. Both LSPR wavelengths and spectral line shapes of the calculated extinction spectra were in very good agreement with the experimental results shown in Figure 2A. We also calculated the integrated $|E/E_0|^4$ on Au concave nanocubes with indentation angle of 140° and various edge lengths at 785 nm excitation. As shown in Figure 4B, better coupling between the LSPRs and excitation laser, in general, gave rise to stronger field enhancements; however, the largest integrated field enhancements were obtained on the 97 nm concave nanocube whose LSPR extinction peak was blue-shifted in comparison to the excitation laser wavelength. This trend was in excellent agreement with our size-dependent spSERS results shown in Figure 2. Since the FDTD calculations considered only individual particles, the offset between the far-field extinction and near-field peak wavelengths should not be

interpreted as the consequence of light extinction in colloidal samples as previously claimed by Murphy and co-workers.[48] Our spSERS results on plasmonically tunable Au concave nanocubes, together with the FDTD results, provide strong evidence that the red shift of the near-field resonance wavelengths with respect to far-field extinction peaks is an intrinsic characteristic of individual metallic nanostructures. Our FDTD calculations considered only the mesoscopic geometry of the nanoparticles; however, atomic-level surface structural details were not included. Whether the atomic steps and kinks present on the high-index facets provide an additional contribution to the overall SERS enhancements is still an open question. Also shown in Figure 4B is the comparison between integrated $|E/E_0|^4$ of Au nanocubes and concave nanocubes of the same edge lengths. It is apparent that concave nanocubes exhibited significantly stronger field enhancements than nanocubes of the same sizes. Size-dependent SERS performances of individual Au nanocubes, however, were not further investigated experimentally, due to the significant corner truncations and limited size tuning range (from ~20 to ~60 nm) of experimentally fabricated Au nanocubes.

2.3. Au Nanotrisoctahedra. A trisoctahedral nanoparticle comprises eight trigonal pyramids generated by "pulling out" the centers of the eight triangular {111} facets of a nanooctahedron. This interesting particle geometry could be visualized in the SEM images shown in Figure 5A, B. Although some of the nanoparticles did not appear trisoctahedral at first glance due to different orientations, a careful survey of particle shapes over a large sample area in a low-magnification SEM image (Figure S5A in Supporting Information) showed that around 90% of the nanoparticles had the trisoctahedral morphology, around 4% of the particles exhibited slightly elongated bipyramidal morphology, and the rest (~6% of the particles) were multifaceted polyhedra with ill-defined facets and overall shapes. Figure 5C shows a TEM image of one individual Au nanotrisoctahedron projected from the [011] zone axis. At this orientation, four out of the 24 facets of the nanotrisoctahedron were projected edge-on and the Miller indices of the exposed facets of the nanotrisoctahedron were determined to be {221} through an analysis of the projection angles marked in Figure 5C.[51,52,55,58] The Au nanotrisoctahedra fabricated by this seed-mediated growth method have essentially the same facets as those obtained from the previously reported one-step seedless approach.[55] The seeded growth method allowed us to fine-tune the size of the nanotrisoctahedra by adjusting the amount of Au seeds added into the growth solutions. As shown in Figure 5D−J, average sizes of the Au nanotrisoctahedra progressively increased as the amount of Au seeds decreased and could be tightly controlled in the range from ~50 nm to over 200 nm. Similar to the Au concave nanocubes, the as-fabricated nanotrisoctahedra could also be immobilized onto poly(4-vinylpyridine)-functionalized glass substrates as a submonolayer of isolated particles for the spSERS measurements (Figure S5B,C in Supporting Information).

Figure 6A shows the extinction spectra of colloidal Au nanotrisoctahedra with various average sizes at a particle concentration of ~1.0 × 10⁹ particles·mL⁻¹. As the particle size increased, the dipolar LSPR progressively red-shifted and became increasingly broadened. For nanotrisoctahedra within the sub-100 nm size regime, only one dipolar LSPR was observed in the extinction spectra. A narrower quadrupolar LSPR emerged at shorter wavelength to the dipole and became
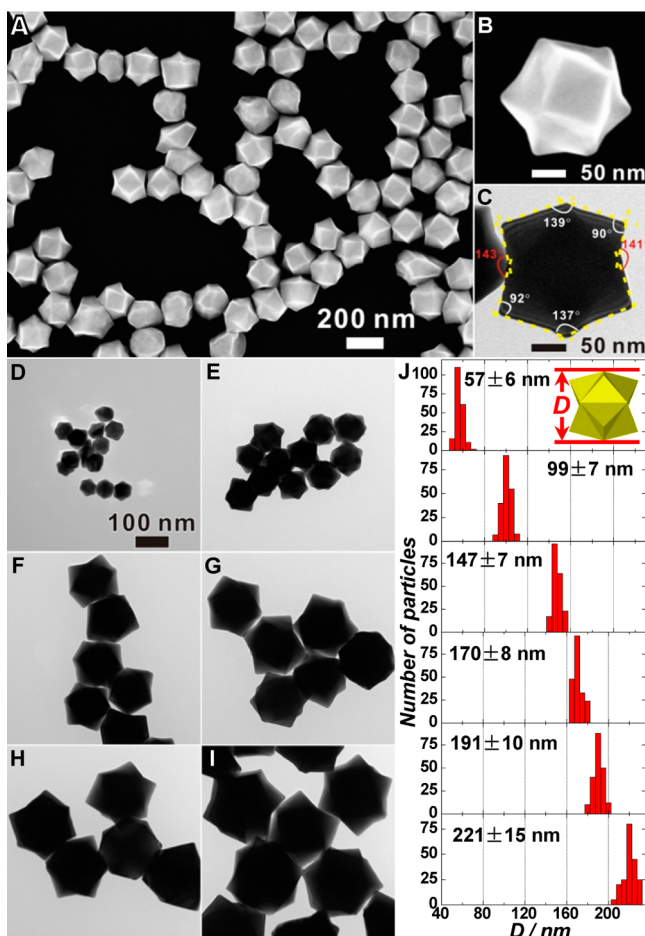
Figure 5. (A) SEM image of Au nanotrisoctahedra with average size, D, of 191 nm. (B) SEM image of one nanotrisoctahedron. (C) TEM image of one individual nanotrisoctahedron with the electron beam projected along the [011] direction. Measured angles between the various edges of the nanotrisoctahedron are marked. (D–I) TEM images of Au nanotrisoctahedra with various average sizes fabricated by adding (D) 0.5, (E) 0.1, (F) 0.05, (G) 0.025, (H) 0.015, and (I) 0.01 mL of Au seed solution. (J) Histograms showing the size distributions of Au nanotrisoctahedra shown in panels D–I.

Figure 6. (A) Experimental extinction spectra of colloidal Au nanotrisoctahedra of various sizes at a particle concentration of ~1.0 × 10^9 particles·mL^−1. Vertical dashed line shows the excitation laser wavelength (785 nm) for Raman measurements. (B) Representative SERS spectra of 4-ATP adsorbed on individual nanotrisoctahedra of various sizes. (C) Histograms of the Raman intensities of 1078 and 1590 cm^−1 modes obtained from individual nanotrisoctahedra. (D) SERS enhancement factors (EF) on individual nanotrisoctahedra at 785 nm excitation. Labels i−vi in all panels correspond to nanotrisoctahedron samples shown in Figure 5D−I, respectively.

increasingly pronounced as the size of the nanotrisoctahedra further increased to beyond 100 nm due to the phase retardation effects.[29] Although higher-order multipolar plasmon modes are generally nonradiative, they absorb light and decay through evanescent near-field, and thus may also contribute to SERS enhancements.[65] While the quadrupole was less sensitively dependent on particle size, the broad dipole band could be systematically shifted with respect to the excitation laser by changing the particle sizes. When used as spSERS substrates, the glass substrates exhibited minimal effects on the plasmon resonance frequencies of the nanotrisoctahedra, as shown in Figure S6 in Supporting Information. Figure 6B shows the representative SERS spectra of 4-ATP SAMs formed on individual Au nanotrisoctahedra of various sizes. Similar to the results obtained on Au concave nanocubes, maximum SERS signals were obtained on the sample whose far-field plasmon band position was blue-shifted by ~70 nm in wavelength with respect to the excitation laser, further verifying that the red shift of optimal excitation wavelength with respect to LSPR extinction peak is a universal phenomenon for metallic nanoparticles of different geometries. We repeated the spSERS
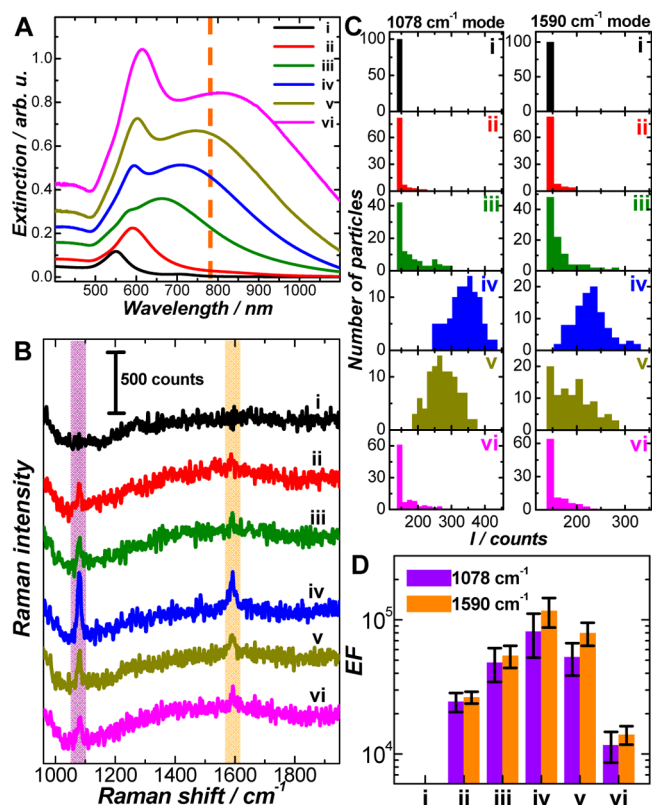
measurements on 100 individual nanotrisoctahedra for each sample, and the histograms of intensities of the 1078 and 1590 cm^−1 modes are shown in Figure 6C. The nanotrisoctahedra exhibited average SERS EFs of ~10^5 when their LSPRs were optimized under 785 nm excitation, and the off-resonance enhancements were generally below 10^4. Although the Au nanotrisoctahedra showed SERS enhancements 1 order of magnitude weaker than those achieved on Au concave nanocubes, they were significantly more efficient as substrates for spSERS than quasi-spherical nanoparticles of the same sizes,[58] primarily due to their tipped surface features. The surface tips of the nanotrisoctahedra were less sharp than those of the concave nanocubes, which may be one of the main reasons why Au nanotrisoctahedra showed lower SERS enhancements than concave nanocubes.

We also used FDTD to calculate the size-dependent far-field extinction spectra and near-field enhancements of individual Au nanotrisoctahedra. The extinction spectra were calculated and averaged over X- and Y-polarizations, as illustrated in the inset of Figure 7A. Integrated near-field enhancements were obtained by integrating the electric field intensities in a sphere of radius $D/2 + 1.5$ nm, where D is the particle size of nanotrisoctahedra. As shown in Figure 7A, calculated extinction spectra of the nanotrisoctahedra were in excellent agreement with the experimental results shown in Figure 6A. Calculated results
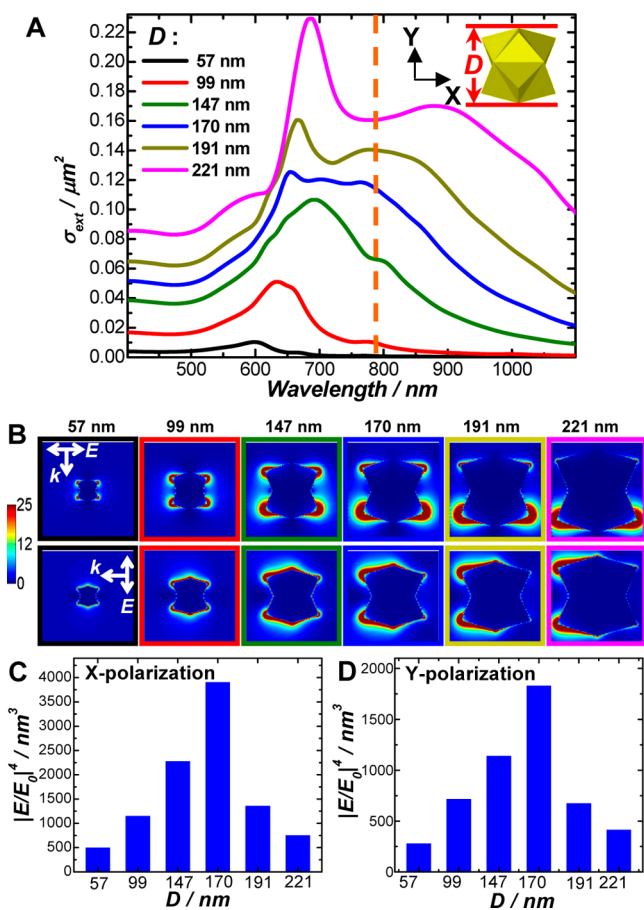
Figure 7. (A) Calculated extinction spectra of Au nanotrisoctahedra of various particle sizes as labeled in the figure. Vertical dashed line shows the excitation laser wavelength (785 nm) for Raman measurements. (B) Cross-sectional views of the calculated near-field enhancements ($|E/E_0|^2$) of Au nanotrisoctahedra with various sizes at 785 nm excitation. (Upper panel) X-polarization; (lower panel) Y-polarization. (C, D) Fourth power of the field enhancements integrated over volume ($|E/E_0|^4$) of Au nanotrisoctahedra with various sizes for (C) X-polarization and (D) Y-polarization.

growth in the presence of surface stabilizers, such as poly(vinylpyrrolidone) (PVP) and cetyltrimethylammonium bromide (CTAB).[35−38] Our protocol of size-controlled synthesis of Au nanostars was essentially the same as that for the concave nanocubes except that multitwinned Au seeds were used instead of single-crystalline seeds. As shown in Figure 8A,
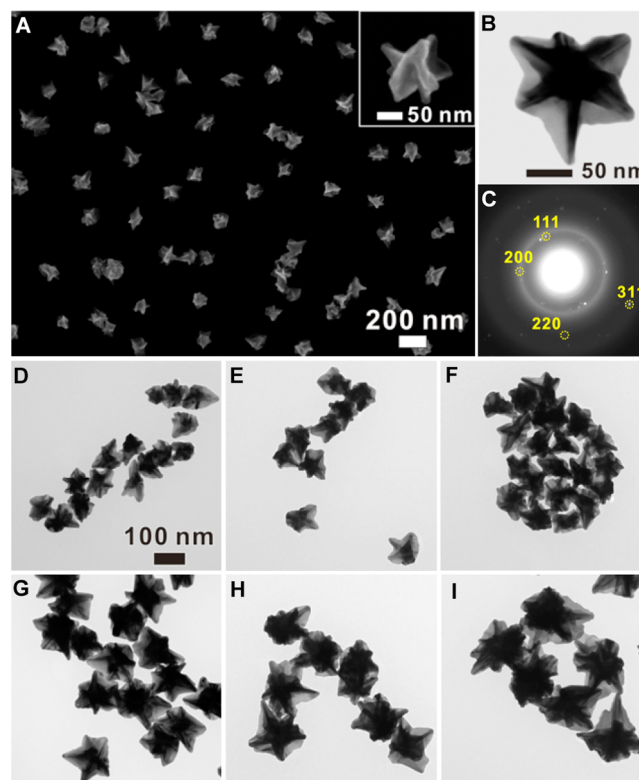

Figure 8. (A) SEM image of Au nanostars fabricated by adding 0.025 mL of Au seed solution. (Inset) One individual Au nanostar. (B) TEM image of one Au nanostar. (C) SAED pattern obtained from the particle shown in panel B. (D−I) TEM images of Au nanostars with different average sizes fabricated by adding (D) 0.5, (E) 0.1, (F) 0.05, (G) 0.025, (H) 0.015, and (I) 0.01 mL of Au seed solution.

on the near-field enhancements (Figure 7B-D) clearly showed that the largest integrated field enhancements were achieved on the 170 nm nanotrisoctahedron whose dipolar LSPR was on the blue side of the excitation laser, though the dipolar LSPR of the 191 nm nanotrisoctahedron better matched the laser wavelength. We have further studied the effects of facet convexity on the far-field and near-field properties of a nanooctahedron (D = 170 nm). As shown in Figure S7 in Supporting Information, the convex nanotrisoctahedron exhibited red-shifted and broadened LSPRs in comparison to the nanooctahedron. The integrated near-field enhancements on the nanotrisoctahedron were several times larger than on the nanooctahedron at 785 nm excitation, indicating that introducing convexity to the nanooctahedron surfaces would give rise to improved SERS enhancements.

2.4. Au Nanostars. Au nanostars are multibranched nanoparticles with geometrically tunable LSPRs and strong electromagnetic field enhancements exploitable for SERS.[35−38] Au nanostars with different sizes, number of branches, and tip sharpness have been chemically synthesized through seedless reduction of gold(III) chloride with 4-(2-hydroxyethyl)-1-piperazineethanesulfonic acid (HEPES)[66] or seed-mediated

the as-fabricated Au nanostars were highly monodisperse in terms of overall particle sizes and multibranched morphology, while tip sharpness and relative orientations of the branches on each nanostar varied form particle to particle. Our method allowed for the fabrication of Au nanostars with nearly 100% yield as revealed by SEM images taken over large sample areas (Figure S8A in Supporting Information). The number of branches on each nanostar varied from 6 to 10, which was determined by the number of facets exposed on the multitwinned Au seeds. In contrast to the single-crystalline Au concave nanocubes and nanotrisoctahedra, the Au nanostars had multitwinned crystalline structures, as revealed by TEM image and SAED pattern shown in Figure 8 panels B and C, respectively. The overall size of Au nanostars could be controlled by adjusting the amount of multitwinned Au seeds added into the growth solutions (Figure 8D−I). Both the average tip sharpness and average number of branches on each nanostar remained unchanged for nanostars with different overall sizes.

The control over the size of Au nanostars allowed us to fine-tune the LSPRs over a broad spectral region across the visible and near-infrared (Figure 9A). As the nanostars became larger
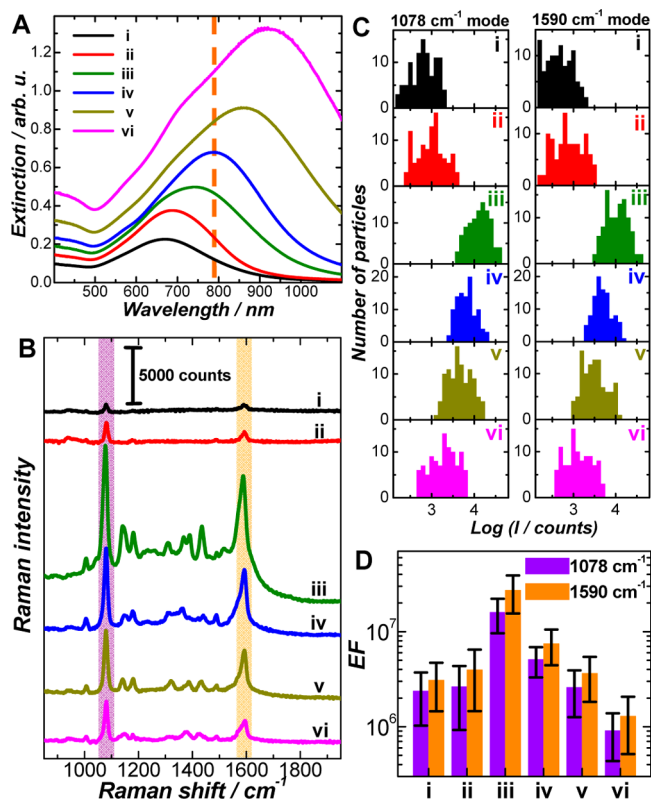
Figure 9. (A) Experimental extinction spectra of colloidal Au nanostars of various sizes at a particle concentration of ~1.0 × 10^9 particles·mL^{-1}. Vertical dashed line shows the excitation laser wavelength (785 nm) for Raman measurements. (B) Representative SERS spectra of 4-ATP adsorbed on individual Au nanostars of various sizes. (C) Histograms of Raman intensities of 1078 and 1590 cm^{-1} modes obtained from individual Au nanostars. (D) SERS enhancement factors (EF) on individual nanostars at 785 nm excitation. Labels i−vi in all panels correspond to nanostar samples shown in Figure 8D−I, respectively.

in size, their LSPR progressively red-shifted and became more intense due to the increase in the particles' extinction cross sections. The plasmonic tunability of nanostars results from the hybridization of plasmons localized at the core and the tips of the nanoparticles.[67] The red shift in LSPRs can be interpreted as the result of increasing aspect ratios of the branches. Similar to the case of Au concave nanocubes and nanotrisoctahedra, spSERS measurements were performed on submonolayers of isolated nanostars immobilized on poly(4-vinylpyridine)-functionalized glass substrates (Figure S8B,C in Supporting Information). Red shift of optimal excitation wavelength with respect to LSPR extinction peak was also observed for Au nanostars. As shown in Figure 9B,C, the nanostar sample with far-field extinction peak at ~740 nm exhibited the largest SERS enhancements. The surface-averaged Raman EFs on individual nanostars were on the order of 10^6 for off-resonance excitations and well exceeded 10^7 when the LSPR was optimized with respect to the excitation laser. The tips of nanostars were sharper than those of the concave nanocubes, giving rise to stronger field enhancements on each tip of the nanostars. In addition, the cores of the nanostars also displayed strong plasmonic antenna effects, dramatically increasing the excitation cross-section and the electromagnetic field enhancements of the tip plasmons.[67,68] Therefore, the SERS enhancements

observed on individual nanostars were approximately 1 order of magnitude higher than those on individual concave nanocubes.

To quantitatively understand the geometry dependence of LSPRs and SERS performance of Au nanostars, we performed FDTD calculations on Au nanostars with various numbers and sizes of tipped branches. The nanostar geometries used for FDTD calculations were taken with conical branches with a tip radius of 5 nm and a tip angle of 30°. Extinction spectra were calculated and averaged for 6, 8, and 10 branches and over two different orthogonal polarizations (X- and Y-polarizations). Figure 10A shows calculated extinction spectra of Au nanostars
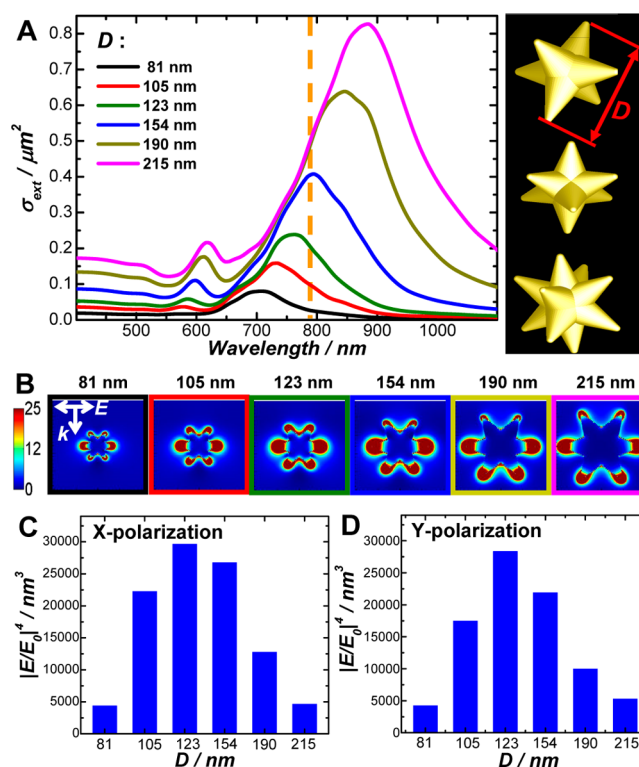

Figure 10. (A) Calculated extinction spectra of individual Au nanostars with varying tip-to-tip distance, D, as labeled in the figure. The right panel shows the geometries of Au nanostar with 6, 8, and 10 branches. Calculated extinction spectra were averaged over different branch numbers and various polarizations. Vertical dashed line shows the excitation laser wavelength (785 nm) for Raman measurements. (B) Cross-sectional views of the calculated near-field enhancements (|E/E$_0$|^2) of Au nanostars with various sizes at 785 nm excitation. (C, D) Fourth power of field enhancements integrated over volume (|E/E$_0$|^4) of Au nanostars with various sizes for (C) X-polarization and (D) Y-polarization.

with various sizes, which are in very good agreement with the experimental results shown in Figure 9A. It was found that the length of the branches had a major effect on LSPR frequencies of the nanostars, with longer branches resulting in more red-shifted LSPRs. LSPR wavelengths of nanostars were also dependent on the thickness of the tipped branches. As shown in Figure S9 in Supporting Information, decreasing thickness of the branches (or tip angle) led to a red shift of the LSPRs. The dependence of nanostar LSPRs on the length and thickness of the branches can be interpreted in the context of the well-understood longitudinal nanorod plasmon, whose resonance wavelength red-shifts as the particle aspect ratio increases.[69] Interestingly, the number of branches per nanostar had minimal

effects on the LSPRs. Increasing the number of branches from 6 to 10 resulted in only slight broadening of the LSPR band, while the LSPR peak positions were essentially unchanged (Figure S10 in Supporting Information), consistent with previous works.[68] Figure 10B−D shows the calculated near-field distributions and integrated field enhancements of Au nanostars of various sizes at 785 nm excitation. Integrated near-field enhancements were obtained by integrating the electric field in a sphere of radius $D/2 + 1.5$ nm, where D is the particle size of nanostar (twice the length of each branch). Once again, the largest integrated field-enhancement was obtained on the nanostar with LSPR band blue-shifted from the excitation laser wavelength (Figure 10C,D), which matched the experimental results on spSERS shown in Figure 9D. The calculated integrated field-enhancements on Au nanostars were about 1 order of magnitude higher than those on Au concave nanocubes, also in excellent agreement with the experimental observations. While significant substrate effects on LSPRs may exist due to the close proximity of tipped branches to the substrate, the relatively uniform distributions of branches around the nanostar core tend to average out the substrate effects.[68] Therefore, substrate effects on Au nanostar plasmons in this case became negligible, which was further verified by the experimental extinction spectra of surface-immobilized nanostars shown in Figure S11 in Supporting Information.

3. CONCLUSIONS

In summary, we have demonstrated that Au concave nanocubes, nanotrisoctahedra, and nanostars with fine-controlled particle sizes and narrow size distributions can be fabricated by a robust solution-phase, seed-mediated growth method through deliberate control over nanoparticle growth kinetics, surface passivation by Ag^+, or crystalline structures (single-crystalline vs multitwinned) of the Au seeds. The capability to precisely control the particle size in each geometry allows us to fine-tune the particle LSPRs with respect to the excitation laser wavelength and quantitatively evaluate the performance of individual nanoparticles as SERS substrates. Our spSERS results, further corroborated by FDTD calculations, provide strong evidence that the red shift of the near-field enhancement peak wavelengths from the far-field LSPR extinction peaks is a universal intrinsic feature of individual metallic nanoparticles of different geometries. Au nanostars, concave nanocubes, and nanotrisoctahedra exhibit SERS enhancements on the order of 10^7, 10^6, and 10^5, respectively, on individual particles at 785 nm excitation when their LSPRs are tuned to the optimal spectral regions with respect to the excitation laser. Our experimental and FDTD results show that individual Au nanoparticles with nanoengineered surface tips may provide plasmonic field enhancements that are sufficiently high for spSERS without involving the strongly coupling plasmons confined in nanoscale interparticle or intraparticle junctions. The knowledge gained through this work provides important information that may guide the design and fabrication of metallic nanoparticles with increasing geometric complexity and further optimized plasmonic properties for SERS-based biosensing and bioimaging applications.

4. METHODS

4.1. Materials. Gold(III) chloride trihydrate ($HAuCl_4 \cdot 3H_2O$, ACS grade) was purchased from J.T. Baker. Sodium borohydride ($NaBH_4$, 99%), L-ascorbic acid (AA, 99.5+%), hydrochloric acid (HCl, 37%), and poly(4-vinylpyridine) (PVP, $M_w \sim 60\,000$) were obtained from

Sigma−Aldrich. Silver nitrate ($AgNO_3$, 99.9995% metals basis), (1-hexadecyl)trimethylammonium chloride (CTAC, 96%), and 4-amino-thiophenol (C_6H_7NS, 4-ATP, 97%) were obtained from Alfa Aesar. Hydrogen peroxide (H_2O_2, 30%), sulfuric acid (H_2SO_4, 96.10%), and ethanol (200 proof) were purchased from Fisher Scientific. All reagents were used as received without further purification. Glass microscope slides were obtained from Gold Seal Products (Portsmouth, NH). Ultrapure water (18.2 MΩ resistivity, Barnstead EasyPure II 7138) was used for all experiments.

4.2. Synthesis of Au Seeds. Colloidal Au seeds were prepared by reducing $HAuCl_4$ with appropriate amounts of $NaBH_4$ in the presence of CTAC. In a typical procedure for single-crystalline Au seed ($\sim$2 nm in diameter) preparation, 0.30 mL of ice-cold, freshly prepared 10 mM $NaBH_4$ was quickly injected into a solution composed of CTAC (10.00 mL, 0.10 M) and $HAuCl_4$ (0.25 mL, 10 mM) under magnetic stirring (1200 rpm). The seed solution was stirred for 1 min and then left undisturbed for 2 h. The seed solution was diluted 1000-fold with CTAC (0.10 M), and the diluted seed solution was used for subsequent seed-mediated growth. For preparation of multitwinned Au seeds ($\sim$3.5 nm in diameter), the volume of 10 mM $NaBH_4$ added into the $HAuCl_4$−CTAC solution was increased to 0.60 mL while all other experimental conditions remained unchanged.

4.3. Synthesis of Au Concave Nanocubes. Au concave nanocubes were prepared following a previous protocol based on seed-mediated growth[56] with minor modifications. The growth solution was prepared by sequentially adding $HAuCl_4$ (0.50 mL, 10 mM), $AgNO_3$ (0.1 mL, 10 mM), HCl (0.20 mL, 1.0 M), and AA (0.10 mL, 0.10 M) into a CTAC (10.00 mL, 0.10 M) solution. After the growth solution was gently mixed for 30 s, growth of Au concave nanocubes was initiated by adding diluted single-crystalline Au seed solution. The reaction solution was gently mixed for 30 s and then left undisturbed at room temperature for 4 h. The obtained Au concave nanocubes were washed with water twice through centrifugation/redispersion cycles and finally redispersed in 5.0 mL of water. The overall sizes of the resulting Au concave nanocube were controlled by adjusting the amount of Au seeds added.

4.4. Synthesis of Au Nanotrisoctahedra. Au nanotrisoctahedra were prepared following a seed-mediated growth method we recently published.[58] The growth solution was prepared by sequentially adding $HAuCl_4$ (0.50 mL, 10 mM) and AA (1.0 mL, 0.10 M) into a CTAC (10.00 mL, 0.10 M) solution. After the growth solution was gently mixed for 30 s, growth of Au nanotrisoctahedra was initiated by adding diluted single-crystalline Au seed solution. The reaction solution was gently mixed for 30 s and then left undisturbed at room temperature for 4 h. The obtained Au nanotrisoctahedra were washed with water twice through centrifugation/redispersion cycles and finally redispersed in 5.0 mL of water. The overall sizes of the resulting Au nanotrisoctahedra were controlled by adjusting the amount of Au seeds added.

4.5. Synthesis of Au Nanostars. Au nanostars were prepared under the same conditions as concave nanocubes except that multitwinned Au seeds were used instead of single-crystalline Au seeds. Briefly, the growth solution was prepared by sequentially adding $HAuCl_4$ (0.50 mL, 10 mM), $AgNO_3$ (0.1 mL, 10 mM), HCl (0.20 mL, 1.0 M), and AA (0.10 mL, 0.10 M) into a CTAC (10.00 mL, 0.10 M) solution. After the growth solution was gently mixed for 30 s, growth of Au nanostars was initiated by adding diluted multitwinned Au seed solution. The reaction solution was gently mixed and then left undisturbed at room temperature for 4 h. The obtained Au nanostars were washed with water twice through centrifugation/redispersion cycles and finally redispersed in 5.0 mL of water. The overall sizes of the resulting Au nanostars were controlled by adjusting the amount of Au seeds added.

4.6. Characterization. TEM and SAED measurements were performed on a Hitachi H-8000 transmission electron microscope operated at an accelerating voltage of 200 kV. SEM images were obtained by use of a Zeiss Ultraplus thermal field emission scanning electron microscope. Optical extinction spectra of the nanoparticles were measured on aqueous colloidal suspensions or surface-immobilized submonolayers of nanoparticles immersed in water at

room temperature, by use of a Beckman Coulter Du 640 spectrophotometer. Raman spectra and dark-field optical microscopy images were obtained on a Bayspec Nomadic Raman microscope built on an Olympus BX51 microscope equipped with a 785 nm CW diode laser.

4.7. spSERS Measurements. Submonolayer films of isolated Au nanoparticles were prepared by immobilizing the particles onto poly(4-vinylpyridine)-functionalized glass substrates. In a typical procedure, glass slides were cleaned in piranha solution (sulfuric acid/H_2O_2 = 7:3) for 15 min and then immersed in 1wt % poly(4-vinylpyridine) ethanolic solution for 24 h. The glass slides were thoroughly rinsed with ethanol, dried with N_2 gas, and then immersed in colloidal suspensions of Au nanoparticles (1.0×10^9 particles·mL^{-1}) for 1 h. The glass slides were thoroughly rinsed with ethanol and dried with N_2 gas after they were removed from the colloidal suspensions of Au nanoparticles. Coverage of Au nanoparticles on the substrates can be controlled by changing the immersion time.

Samples for spSERS experiments were prepared by evaporating 20 μL of a 1.0 mM ethanolic solution of 4-ATP on the surfaces of the isolated Au nanoparticles on poly(4-vinylpyridine)-functionalized glass substrates. The substrates were then thoroughly rinsed with ethanol and dried with N_2 gas. Water was dropped onto the substrates to ensure that the surrounding medium of the Au nanoparticles was water, and then a clean glass coverslip with 0.17 mm thickness was covered onto the top of the water layer before the Raman spectral collection. The distance between the two glass slides was about 0.5 mm. SERS spectra were obtained on a Bayspec Nomadic Raman microscope built on an Olympus BX51 reflected optical system equipped with a 785 nm CW diode excitation laser using the confocal mode (focal area of 1 μm in radius). A 50× dark-field objective (NA = 0.5, WD = 10.6 mm, Olympus LMPLFLN-BD) was used for both Raman signal collection and dark-field scattering imaging. The laser beam was focused on one particle each time for Raman spectrum collection. The laser power focused on the samples was measured to be 3.6 mW, and the spectrum acquisition time was 20 s. Normal Raman spectra of 4-ATP were collected on a solid film of neat 4-ATP on a glass slide. Details of normal Raman measurements on 4-ATP were reported in a paper we recently published.[58]

4.8. Enhancement Factor Calculations. We estimated the enhancement factors (EFs) of Raman signals from the following equation:

$$\text{EF} = \frac{I_{\text{SERS}} N_{\text{normal}}}{I_{\text{normal}} N_{\text{SERS}}}$$

where I_{SERS} is the intensity of a specific band in the SERS spectra of 4-ATP; I_{normal} is the intensity of the same band in the normal Raman spectra of 4-ATP under the same conditions; N_{normal} is the number of probe molecules in the excitation volume for the normal Raman measurements; and N_{SERS} is the number of adsorbed molecules on an individual particle. Two Raman modes of 4-ATP at 1078 and 1590 cm^{-1} were chosen for the EF calculations. To estimate N_{normal}, we calculated the effective excitation volume by using the following equation:

$$V = \pi(d/2)^2 H$$

where d is the diameter of the beam size ($d = 2$ μm) and H is the effective depth of focus ($H = 10$ μm, which was estimated by finely controlling the height of the stage during the Raman measurements). We estimated an effective excitation volume of 3.14×10^{-17} m^3 for our Raman microscopy with 785 nm excitation using the 50× objective. N_{normal} was calculated by using the following expression:

$$N_{\text{normal}} = (VD/M)N_{\text{A}} = 1.80 \times 10^{11} \text{ molecules}$$

where D is the density of 4-ATP (1.17 g/mL), M is the molar mass of 4-ATP (125 g/mol), and $N_{\text{A}} = 6.02 \times 10^{23}$ mol^{-1} is the Avogadro constant. To determine N_{SERS}, a self-assembled monolayer of 4-ATP molecules (molecular footprint size 0.39 nm^2)[63] was assumed to be closely packed on the surface of each Au particle. The surface area of the particle was estimated as follows: (1) For Au concave nanocubes,

when the indentation angle is 140°, the surface area were calculated as $S = 6D^2[1/\sin(70°)]$. (2) For Au nanotrisoctahedra, the surface area was calculated as $S = 7.09D^2$. (3) For Au nanostars, the surface area was roughly calculated as $S = 1.52D^2$. In this way we were able to estimate N_{SERS} values on nanoparticles with different sizes and then calculate the EFs.

4.9. Finite-Difference Time-Domain Calculations. FDTD calculations were performed by use of a commercial FDTD software package (Lumerical Solutions). Dielectric permittivity tabulated by Johnson and Christy[70] was used for Au. Geometric parameters used in the simulations for Au concave nanocubes, nanotrisoctahedra, and nanostars were extracted from the experimental TEM and SEM images. FDTD calculations were performed on single nanoparticles in water (refractive index of 1.34). The near-field enhancements were calculated for an excitation at 785 nm in all cases. To account for small morphological details and ensure good numerical convergence, a uniform FDTD mesh grid of 1 nm was used.

■ ASSOCIATED CONTENT

Ⓢ Supporting Information

Eleven figures showing low-magnification SEM images and dark-field optical microscopy and SEM images of submonolayers of isolated Au concave nanocubes, nanotrisoctahedra, and nanostars; experimental extinction spectra of aqueous colloidal and surface-immobilized Au concave nanocubes, nanotrisoctahedra, and nanostars; SERS spectra of 4-ATP SAMs on Au concave nanocubes; normal Raman spectrum of pure 4-ATP solid film; calculated extinction spectra and near-field enhancements of Au nanooctahedron and nanotrisoctahedron; and calculated extinction spectra of Au nanostars with different branch thicknesses and numbers of branches. This material is available free of charge via the Internet at http://pubs.acs.org.

■ AUTHOR INFORMATION

Corresponding Author
*E-mail wang344@mailbox.sc.edu; phone 803-777-2203; fax 803-777-9521.

Present Address
§Department of Chemistry, Northwestern University, Evanston, IL 60208.

Notes
The authors declare no competing financial interest.

■ ACKNOWLEDGMENTS

■ REFERENCES

(1) Campion, A.; Kambhampati, P. Surface-Enhanced Raman Scattering. *Chem. Soc. Rev.* **1998**, *27*, 241−250.

(2) Stiles, P. L.; Dieringer, J. A.; Shah, N. C.; Van Duyne, R. R. Surface-Enhanced Raman Spectroscopy. *Annu. Rev. Anal. Chem.* **2008**, *1*, 601−626.

(3) Craig, A. P.; Franca, A. S.; Irudayaraj, J. Surface-Enhanced Raman Spectroscopy Applied to Food Safety. *Annu. Rev. Food Sci. Technol.* **2013**, *4*, 369−380.

(4) Li, J. F.; Huang, Y. F.; Ding, Y.; Yang, Z. L.; Li, S. B.; Zhou, X. S.; Fan, F. R.; Zhang, W.; Zhou, Z. Y.; Wu, D. Y.; Ren, B.; Wang, Z. L.; Tian, Z. Q. Shell-Isolated Nanoparticle-Enhanced Raman Spectroscopy. *Nature* **2010**, *464*, 392−395.

(5) Halvorson, R. A.; Vikesland, P. J. Surface-Enhanced Raman Spectroscopy (SERS) for Environmental Analyses. *Environ. Sci. Technol.* **2010**, *44*, 7749−7755.

(6) Shafer-Peltier, K. E.; Haynes, C. L.; Glucksberg, M. R.; Van Duyne, R. P. Toward a Glucose Biosensor Based on Surface-Enhanced Raman Scattering. *J. Am. Chem. Soc.* **2003**, *125*, 588−593.

(7) Anker, J. N.; Hall, W. P.; Lyandres, O.; Shah, N. C.; Zhao, J.; Van Duyne, R. P. Biosensing with Plasmonic Nanosensors. *Nat. Mater.* **2008**, *7*, 442−453.

(8) Alvarez-Puebla, R. A.; Liz-Marzan, L. M. SERS-Based Diagnosis and Biodetection. *Small* **2010**, *6*, 604−610.

(9) Qian, X. M.; Peng, X. H.; Ansari, D. O.; Yin-Goen, Q.; Chen, G. Z.; Shin, D. M.; Yang, L.; Young, A. N.; Wang, M. D.; Nie, S. M. In Vivo Tumor Targeting and Spectroscopic Detection with Surface-Enhanced Raman Nanoparticle Tags. *Nat. Biotechnol.* **2008**, *26*, 83−90.

(10) Doering, W. E.; Piotti, M. E.; Natan, M. J.; Freeman, R. G. SERS as a Foundation for Nanoscale, Optically Detected Biological Labels. *Adv. Mater.* **2007**, *19*, 3100−3108.

(11) Zavaleta, C. L.; Smith, B. R.; Walton, I.; Doering, W.; Davis, G.; Shojaei, B.; Natan, M. J.; Gambhir, S. S. Multiplexed Imaging of Surface Enhanced Raman Scattering Nanotags in Living Mice Using Noninvasive Raman Spectroscopy. *Proc. Natl. Acad. Sci. U.S.A.* **2009**, *106*, 13511−13516.

(12) Maiti, K. K.; Dinish, U. S.; Samanta, A.; Vendrell, M.; Soh, K. S.; Park, S. J.; Olivo, M.; Chang, Y. T. Multiplex Targeted in Vivo Cancer Detection Using Sensitive Near-Infrared SERS Nanotags. *Nano Today* **2012**, *7*, 85−93.

(13) Camden, J. P.; Dieringer, J. A.; Zhao, J.; Van Duyne, R. P. Controlled Plasmonic Nanostructures for Surface-Enhanced Spectroscopy and Sensing. *Acc. Chem. Res.* **2008**, *41*, 1653−1661.

(14) Halas, N. J.; Lal, S.; Chang, W. S.; Link, S.; Nordlander, P. Plasmons in Strongly Coupled Metallic Nanostructures. *Chem. Rev.* **2011**, *111*, 3913−3961.

(15) Wang, H.; Levin, C. S.; Halas, N. J. Nanosphere Arrays with Controlled Sub-10-nm Gaps as Surface-Enhanced Raman Spectroscopy Substrates. *J. Am. Chem. Soc.* **2005**, *127*, 14992−14993.

(16) Lee, S. J.; Morrill, A. R.; Moskovits, M. Hot Spots in Silver Nanowire Bundles for Surface-Enhanced Raman Spectroscopy. *J. Am. Chem. Soc.* **2006**, *128*, 2200−2201.

(17) Wang, H. H.; Liu, C. Y.; Wu, S. B.; Liu, N. W.; Peng, C. Y.; Chan, T. H.; Hsu, C. F.; Wang, J. K.; Wang, Y. L. Highly Raman-Enhancing Substrates Based on Silver Nanoparticle Arrays with Tunable Sub-10 nm Gaps. *Adv. Mater.* **2006**, *18*, 491−495.

(18) Kneipp, K.; Wang, Y.; Kneipp, H.; Perelman, L. T.; Itzkan, I.; Dasari, R.; Feld, M. S. Single Molecule Detection Using Surface-Enhanced Raman Scattering (SERS). *Phys. Rev. Lett.* **1997**, *78*, 1667−1670.

(19) Xu, H. X.; Bjerneld, E. J.; Kall, M.; Borjesson, L. Spectroscopy of Single Hemoglobin Molecules by Surface Enhanced Raman Scattering. *Phys. Rev. Lett.* **1999**, *83*, 4357−4360.

(20) Camden, J. P.; Dieringer, J. A.; Wang, Y. M.; Masiello, D. J.; Marks, L. D.; Schatz, G. C.; Van Duyne, R. P. Probing the Structure of Single-Molecule Surface-Enhanced Raman Scattering Hot Spots. *J. Am. Chem. Soc.* **2008**, *130*, 12616−12617.

(21) Fang, Y.; Seong, N. H.; Dlott, D. D. Measurement of the Distribution of Site Enhancements in Surface-Enhanced Raman Scattering. *Science* **2008**, *321*, 388−392.

(22) Lim, D. K.; Jeon, K. S.; Hwang, J. H.; Kim, H.; Kwon, S.; Suh, Y. D.; Nam, J. M. Highly Uniform and Reproducible Surface-Enhanced Raman Scattering from DNA-Tailorable Nanoparticles with 1-nm Interior Gap. *Nat. Nanotechnol.* **2011**, *6*, 452−460.

(23) Qian, X. M.; Nie, S. M. Single-Molecule and Single-Nanoparticle SERS: From Fundamental Mechanisms to Biomedical Applications. *Chem. Soc. Rev.* **2008**, *37*, 912−920.

(24) Sha, M. Y.; Xu, H. X.; Natan, M. J.; Cromer, R. Surface-Enhanced Raman Scattering Tags for Rapid and Homogeneous Detection of Circulating Tumor Cells in the Presence of Human Whole Blood. *J. Am. Chem. Soc.* **2008**, *130*, 17214−17215.

(25) Lal, S.; Grady, N. K.; Kundu, J.; Levin, C. S.; Lassiter, J. B.; Halas, N. J. Tailoring Plasmonic Substrates for Surface Enhanced Spectroscopies. *Chem. Soc. Rev.* **2008**, *37*, 898−911.

(26) Xia, Y. N.; Halas, N. J. Shape-Controlled Synthesis and Surface Plasmonic Properties of Metallic Nanostructures. *MRS Bull.* **2005**, *30*, 338−344.

(27) Gandra, N.; Singamaneni, S. Bilayered Raman-Intense Gold Nanostructures with Hidden Tags (BRIGHTs) for High-Resolution Bioimaging. *Adv. Mater.* **2013**, *25*, 1022−1027.

(28) Song, J. B.; Duan, B.; Wang, C. X.; Zhou, J. J.; Pu, L.; Fang, Z.; Wang, P.; Lim, T. T.; Duan, H. W. SERS-Encoded Nanogapped Plasmonic Nanoparticles: Growth of Metallic Nanoshell by Templating Redox-Active Polymer Brushes. *J. Am. Chem. Soc.* **2014**, *136*, 6838−6841.

(29) Wang, H.; Halas, N. J. Mesoscopic Au "Meatball" Particles. *Adv. Mater.* **2008**, *20*, 820−825.

(30) Fang, J. X.; Du, S. Y.; Lebedkin, S.; Li, Z. Y.; Kruk, R.; Kappes, M.; Hahn, H. Gold Mesostructures with Tailored Surface Topography and Their Self-Assembly Arrays for Surface-Enhanced Raman Spectroscopy. *Nano Lett.* **2010**, *10*, 5006−5013.

(31) Lin, H. X.; Li, J. M.; Liu, B. J.; Liu, D. Y.; Liu, J. X.; Terfort, A.; Xie, Z. X.; Tian, Z. Q.; Ren, B. Uniform Gold Spherical Particles for Single-Particle Surface-Enhanced Raman Spectroscopy. *Phys. Chem. Chem. Phys.* **2013**, *15*, 4130−4135.

(32) Li, S. W.; Xu, P.; Ren, Z. Q.; Zhang, B.; Du, Y. C.; Han, X. J.; Mack, N. H.; Wang, H. L. Fabrication of Thorny Au Nanostructures on Polyaniline Surfaces for Sensitive Surface-Enhanced Raman Spectroscopy. *ACS Appl. Mater. Interfaces* **2013**, *5*, 49−54.

(33) Liang, H. Y.; Li, Z. P.; Wang, W. Z.; Wu, Y. S.; Xu, H. X. Highly Surface-Roughened "Flower-like" Silver Nanoparticles for Extremely Sensitive Substrates of Surface-Enhanced Raman Scattering. *Adv. Mater.* **2009**, *21*, 4614−4618.

(34) Mulvihill, M. J.; Ling, X. Y.; Henzie, J.; Yang, P. D. Anisotropic Etching of Silver Nanoparticles for Plasmonic Structures Capable of Single-Particle SERS. *J. Am. Chem. Soc.* **2010**, *132*, 268−274.

(35) Barbosa, S.; Agrawal, A.; Rodriguez-Lorenzo, L.; Pastoriza-Santos, I.; Alvarez-Puebla, R. A.; Kornowski, A.; Weller, H.; Liz-Marzan, L. M. Tuning Size and Sensing Properties in Colloidal Gold Nanostars. *Langmuir* **2010**, *26*, 14943−14950.

(36) Rodriguez-Lorenzo, L.; Alvarez-Puebla, R. A.; de Abajo, F. J. G.; Liz-Marzan, L. M. Surface Enhanced Raman Scattering Using Star-Shaped Gold Colloidal Nanoparticles. *J. Phys. Chem. C* **2010**, *114*, 7336−7340.

(37) Khoury, C. G.; Vo-Dinh, T. Gold Nanostars for Surface-Enhanced Raman Scattering: Synthesis, Characterization and Optimization. *J. Phys. Chem. C* **2008**, *112*, 18849−18859.

(38) Hrelescu, C.; Sau, T. K.; Rogach, A. L.; Jackel, F.; Feldmann, J. Single Gold Nanostars Enhance Raman Scattering. *Appl. Phys. Lett.* **2009**, *94*, No. 153113.

(39) Sanchez-Gaytan, B. L.; Swanglap, P.; Lamkin, T. J.; Hickey, R. J.; Fakhraai, Z.; Link, S.; Park, S. J. Spiky Gold Nanoshells: Synthesis and Enhanced Scattering Properties. *J. Phys. Chem. C* **2012**, *116*, 10318−10324.

(40) Wang, H.; Goodrich, G. P.; Tam, F.; Oubre, C.; Nordlander, P.; Halas, N. J. Controlled Texturing Modifies the Surface Topography and Plasmonic Properties of Au Nanoshells. *J. Phys. Chem. B* **2005**, *109*, 11083−11087.

(41) Jackson, J. B.; Halas, N. J. Surface-Enhanced Raman Scattering on Tunable Plasmonic Nanoparticle Substrates. *Proc. Natl. Acad. Sci. U.S.A.* **2004**, *101*, 17930−17935.

(42) McFarland, A. D.; Young, M. A.; Dieringer, J. A.; Van Duyne, R. P. Wavelength-Scanned Surface-Enhanced Raman Excitation Spectroscopy. *J. Phys. Chem. B* **2005**, *109*, 11279−11285.

(43) Ross, B. M.; Lee, L. P. Comparison of Near- and Far-Field Measures for Plasmon Resonance of Metallic Nanoparticles. *Opt. Lett.* **2009**, *34*, 896−898.

(44) Zuloaga, J.; Nordlander, P. On the Energy Shift between Near-Field and Far-Field Peak Intensities in Localized Plasmon Systems. *Nano Lett.* **2011**, *11*, 1280−1283.

(45) Menzel, C.; Hebestreit, E.; Muhlig, S.; Rockstuhl, C.; Burger, S.; Lederer, F.; Pertsch, T. The Spectral Shift between Near- and Far-Field Resonances of Optical Nano-Antennas. *Opt. Express* **2014**, *22*, 9971−9982.

(46) Moreno, F.; Albella, P.; Nieto-Vesperinas, M. Analysis of the Spectral Behavior of Localized Plasmon Resonances in the Near- and Far-Field Regimes. *Langmuir* **2013**, *29*, 6715−6721.

(47) Alonso-Gonzalez, P.; Albella, P.; Neubrech, F.; Huck, C.; Chen, J.; Golmar, F.; Casanova, F.; Hueso, L. E.; Pucci, A.; Aizpurua, J.; Hillenbrand, R. Experimental Verification of the Spectral Shift between Near- and Far-Field Peak Intensities of Plasmonic Infrared Nano-antennas. *Phys. Rev. Lett.* **2013**, *110*, No. 203902.

(48) Sivapalan, S. T.; DeVetter, B. M.; Yang, T. K.; van Dijk, T.; Schulmerich, M. V.; Carney, P. S.; Bhargava, R.; Murphy, C. J. Off-Resonance Surface-Enhanced Raman Spectroscopy from Gold Nano-rod Suspensions as a Function of Aspect Ratio: Not What We Thought. *ACS Nano* **2013**, *7*, 2099−2105.

(49) Chiu, C. Y.; Chung, P. J.; Lao, K. U.; Liao, C. W.; Huang, M. H. Facet-Dependent Catalytic Activity of Gold Nanocubes, Octahedra, and Rhombic Dodecahedra toward 4-Nitroaniline Reduction. *J. Phys. Chem. C* **2012**, *116*, 23757−23763.

(50) Personick, M. L.; Mirkin, C. A. Making Sense of the Mayhem behind Shape Control in the Synthesis of Gold Nanoparticles. *J. Am. Chem. Soc.* **2013**, *135*, 18238−18247.

(51) Yu, Y.; Zhang, Q. B.; Lu, X. M.; Lee, J. Y. Seed-Mediated Synthesis of Monodisperse Concave Trisoctahedral Gold Nanocrystals with Controllable Sizes. *J. Phys. Chem. C* **2010**, *114*, 11119−11126.

(52) Eguchi, M.; Mitsui, D.; Wu, H. L.; Sato, R.; Teranishi, T. Simple Reductant Concentration-Dependent Shape Control of Polyhedral Gold Nanoparticles and Their Plasmonic Properties. *Langmuir* **2012**, *28*, 9021−9026.

(53) Ming, T.; Feng, W.; Tang, Q.; Wang, F.; Sun, L. D.; Wang, J. F.; Yan, C. H. Growth of Tetrahexahedral Gold Nanocrystals with High-index Facets. *J. Am. Chem. Soc.* **2009**, *131*, 16350−16351.

(54) Yin, P. G.; You, T. T.; Tan, E. Z.; Li, J.; Lang, X. F.; Jiang, L.; Guo, L. Characterization of Tetrahexahedral Gold Nanocrystals: A Combined Study by Surface-Enhanced Raman Spectroscopy and Computational Simulations. *J. Phys. Chem. C* **2011**, *115*, 18061−18069.

(55) Ma, Y. Y.; Kuang, Q.; Jiang, Z. Y.; Xie, Z. X.; Huang, R. B.; Zheng, L. S. Synthesis of Trisoctahedral Gold Nanocrystals with Exposed High-Index Facets by a Facile Chemical Method. *Angew. Chem., Int. Ed.* **2008**, *47*, 8901−8904.

(56) Zhang, J.; Langille, M. R.; Personick, M. L.; Zhang, K.; Li, S. Y.; Mirkin, C. A. Concave Cubic Gold Nanocrystals with High-Index Facets. *J. Am. Chem. Soc.* **2010**, *132*, 14012−14014.

(57) Hong, J. W.; Lee, S. U.; Lee, Y. W.; Han, S. W. Hexoctahedral Au Nanocrystals with High-Index Facets and Their Optical and Surface-Enhanced Raman Scattering Properties. *J. Am. Chem. Soc.* **2012**, *134*, 4565−4568.

(58) Zhang, Q. F.; Large, N.; Nordlander, P.; Wang, H. Porous Au Nanoparticles with Tunable Plasmon Resonances and Intense Field Enhancements for Single-Particle SERS. *J. Phys. Chem. Lett.* **2014**, *5*, 370−374.

(59) Huang, Y. J.; Wu, L.; Chen, X. D.; Bai, P.; Kim, D. H. Synthesis of Anisotropic Concave Gold Nanocuboids with Distinctive Plasmonic Properties. *Chem. Mater.* **2013**, *25*, 2470−2475.

(60) Sau, T. K.; Murphy, C. J. Room Temperature, High-Yield Synthesis of Multiple Shapes of Gold Nanoparticles in Aqueous Solution. *J. Am. Chem. Soc.* **2004**, *126*, 8648−8649.

(61) Rycenga, M.; Langille, M. R.; Personick, M. L.; Ozel, T.; Mirkin, C. A. Chemically Isolating Hot Spots on Concave Nanocubes. *Nano Lett.* **2012**, *12*, 6218−6222.

(62) Malynych, S.; Luzinov, I.; Chumanov, G. Poly(vinyl pyridine) as a Universal Surface Modifier for Immobilization of Nanoparticles. *J. Phys. Chem. B* **2002**, *106*, 1280−1285.

(63) Mohri, N.; Matsushita, S.; Inoue, M.; Yoshikawa, K. Desorption of 4-Aminobenzenethiol Bound to a Gold Surface. *Langmuir* **1998**, *14*, 2343−2347.

(64) van Schrojenstein Lantman, E. M.; Deckert-Gaudig, T.; Mank, A. J. G.; Deckert, V.; Weckhuysen, B. M. Catalytic Processes Monitored at the Nanoscale with Tip-Enhanced Raman Spectroscopy. *Nat. Nanotechnol.* **2012**, *7*, 583−586.

(65) Hastings, S. P.; Swanglap, P.; Qian, Z. C.; Fang, Y.; Park, S. J.; Link, S.; Engheta, N.; Fakhraai, Z. Quadrupole-Enhanced Raman Scattering. *ACS Nano* **2014**, *8*, DOI: 10.1021/nn5022346.

(66) Xie, J.; Lee, J. Y.; Wang, D. I. C. Seedless, Surfactantless, High-Yield Synthesis of Branched Gold Nanocrystals in HEPES Buffer Solution. *Chem. Mater.* **2007**, *19*, 2823−2830.

(67) Hao, F.; Nehl, C. L.; Hafner, J. H.; Nordlander, P. Plasmon Resonances of a Gold Nanostar. *Nano Lett.* **2007**, *7*, 729−732.

(68) Das, P.; Kedia, A.; Kumar, P. S.; Large, N.; Chini, T. K. Local Electron Beam Excitation and Substrate Effect on the Plasmonic Response of Single Gold Nanostars. *Nanotechnology* **2013**, *24*, No. 405704.

(69) Link, S.; El-Sayed, M. A. Spectral Properties and Relaxation Dynamics of Surface Plasmon Electronic Oscillations in Gold and Silver Nanodots and Nanorods. *J. Phys. Chem. B* **1999**, *103*, 8410−8426.

(70) Johnson, P. B.; Christy, R. W. Optical Constants of Noble Metals. *Phys. Rev. B* **1972**, *6*, 4370−4379.

17267

dx.doi.org/10.1021/am505245z | *ACS Appl. Mater. Interfaces* 2014, 6, 17255−17267